

Supplemental Material for

Complex Multi-patch Rupture and Aftershock Characteristics of the 2024 M_w 4.2 Buan, Korea, Earthquake Sequence

Min-Seong Seo¹, Won-Young Kim², Sangwoo Han¹, Jun Yong Park¹, YoungHee Kim¹

¹School of Earth and Environmental Sciences, Seoul National University

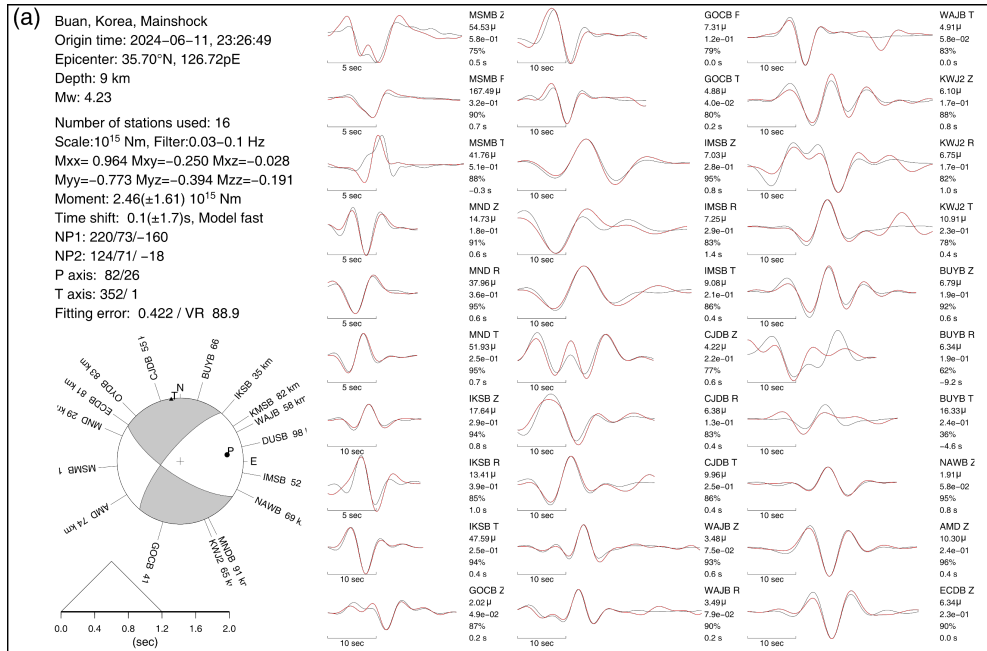
²Lamont-Doherty Earth Observatory of Columbia University

Corresponding author: YoungHee Kim (younghkim@snu.ac.kr)

This supplemental material contains the following items:

- **Figure S1:** Moment tensor inversion result for the mainshock and the largest aftershock (event 17).
- **Figure S2:** Comparison of mainshock RSTFs using multiple EGF candidates.
- **Figure S3:** Comparison of mainshock and reconstructed waveforms obtained by convolution of EGF and RSTF.
- **Figure S4:** Elliptical two-patch models obtained with varying subfault grid sizes and risetimes.
- **Figure S5:** RSTF fitting results from the linear slip inversion.
- **Figure S6:** Summary of the three-patch model.
- **Figure S7:** Rupture models obtained without SmS phases.
- **Figure S8:** Rupture models obtained under limited azimuthal coverage.
- **Figure S9:** Estimated stress drops and rupture areas of the elliptical patches.
- **Figure S10:** Coulomb stress changes calculated with linear inversion slip model.

- **Figure S11:** RSTFs (P , S , SmS) of event 17 (M_L 3.1).
- **Table S1:** Catalog of the 2024 Buan, Korea, earthquake sequence.
- **Table S2:** Second-degree moment parameters and associated uncertainties for event 17.



2024-06-11 Mainshock, Buan, Korea

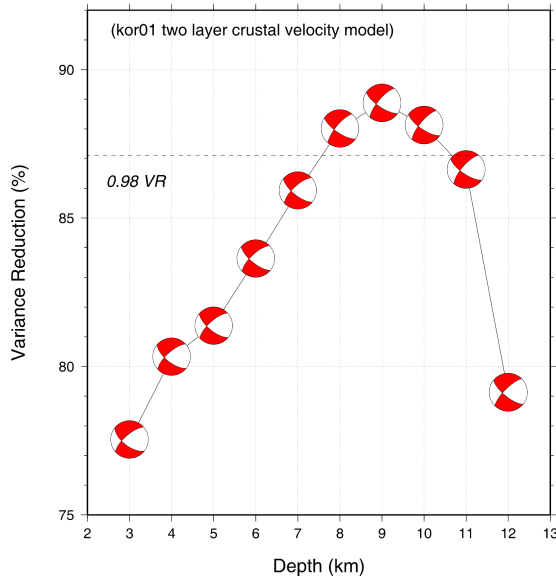


Figure S1a. (top) A comparison of the best fit observed (black traces) and synthetic seismograms (red traces) of the mainshock calculated for a focal depth of 9 km. 3-component records from 16 stations in a distance range of 15 - 98 km are used (12 stations are shown). A two-layer velocity model of Kim and Kim (1983) is used for synthetics. (bottom) Focal depth is constrained by calculating synthetics at 1 km intervals and finding the best-fit depth. Focal depth is well constrained at 9 km with uncertainty of about ± 1 km.

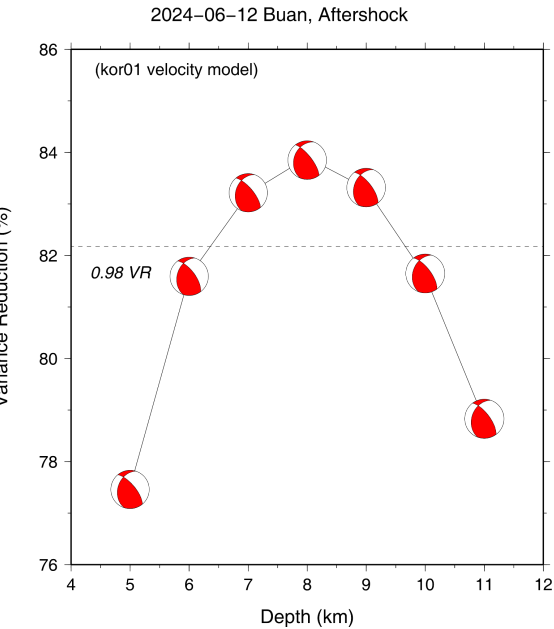
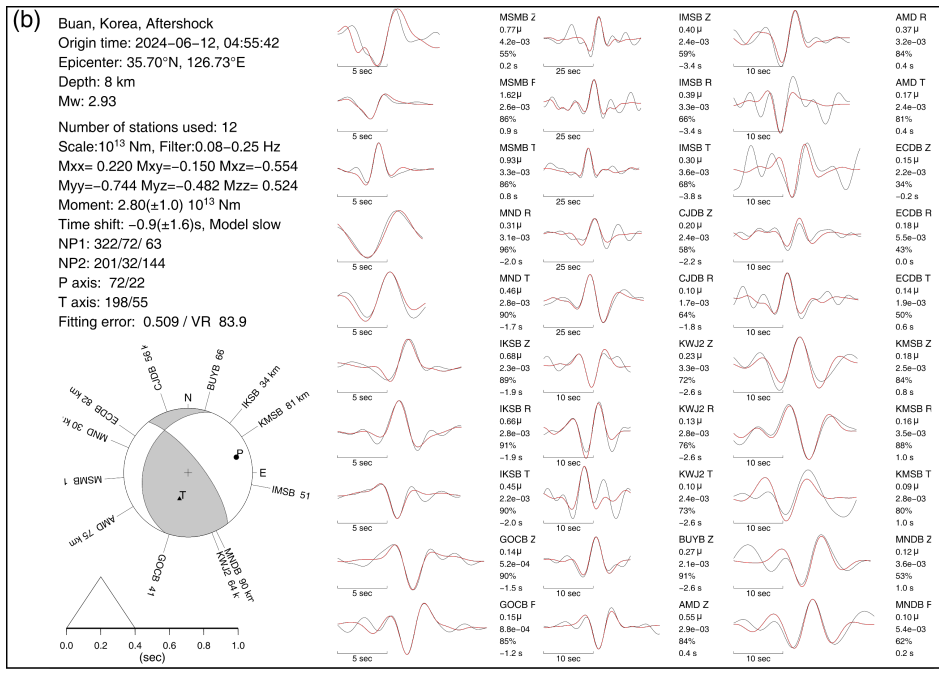
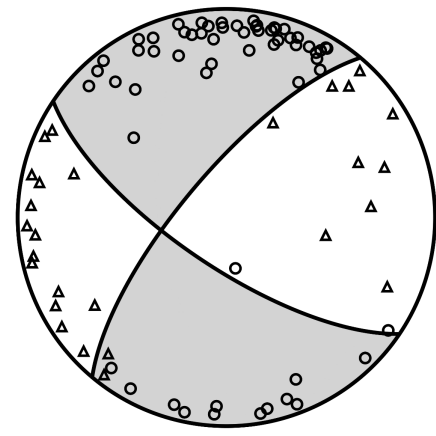
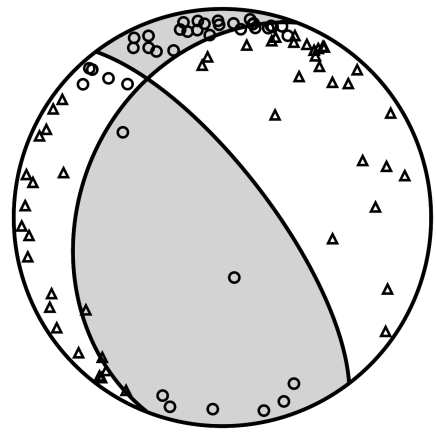


Figure S1b. (top) A comparison of the best fit observed (black traces) and synthetic seismograms (red traces) of event 17 calculated for a focal depth of 8 km. 3-component records from 12 stations in a distance range of 16 - 90 km are used. A two-layer velocity model of Kim and Kim (1983) is used for synthetics. The focal mechanism is a thrust fault. (bottom) Focal depth is constrained by calculating synthetics at 1 km intervals and finding the best-fit depth. Focal depth is well constrained at 8 km with uncertainty of about ± 1 km.

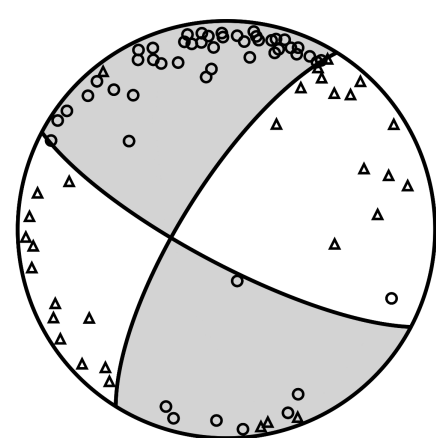
(c) Mainshock (M_w 4.2)



Event no. 17 (M_w 2.9)



Event no. 29 (M_w 2.4)



Event no. 38 (M_w 2.4)

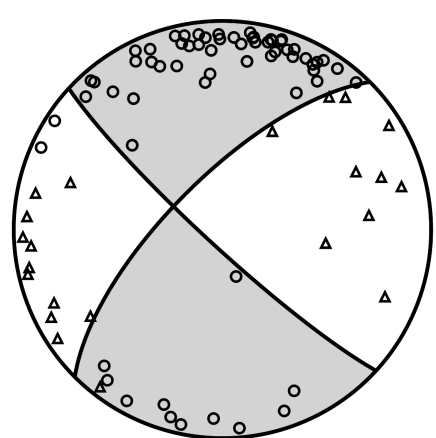


Figure S1c. P -wave first motion polarities and focal mechanisms for four events with $\mathbf{M} \geq 2$.

Empty circles denote upward (compressional) polarities, and empty triangles denote downward (dilatational) polarities.

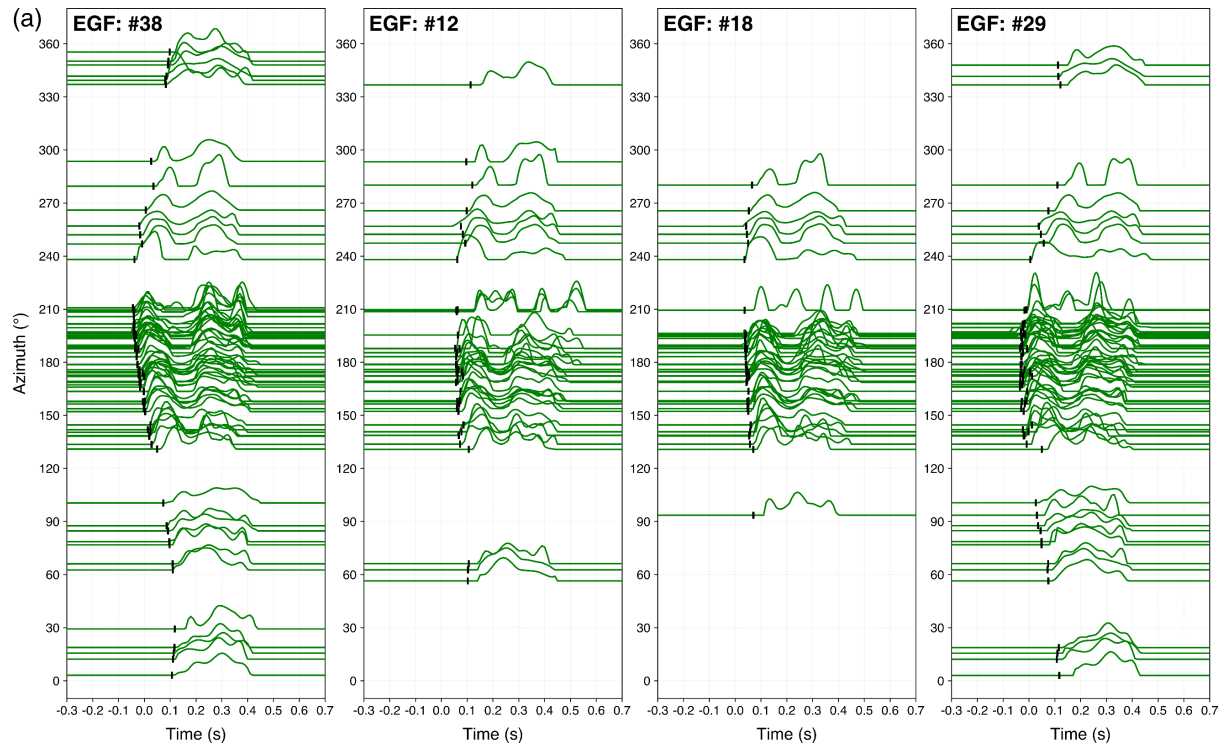


Figure S2a. Direct P -phase mainshock RSTFs obtained using four different EGF candidates (no. 38, 12, 18, and 29). The RSTFs are aligned by station azimuth and normalized by seismic moment. Black vertical bars mark the theoretical differential times calculated based on the relative location between the mainshock and the EGF event.

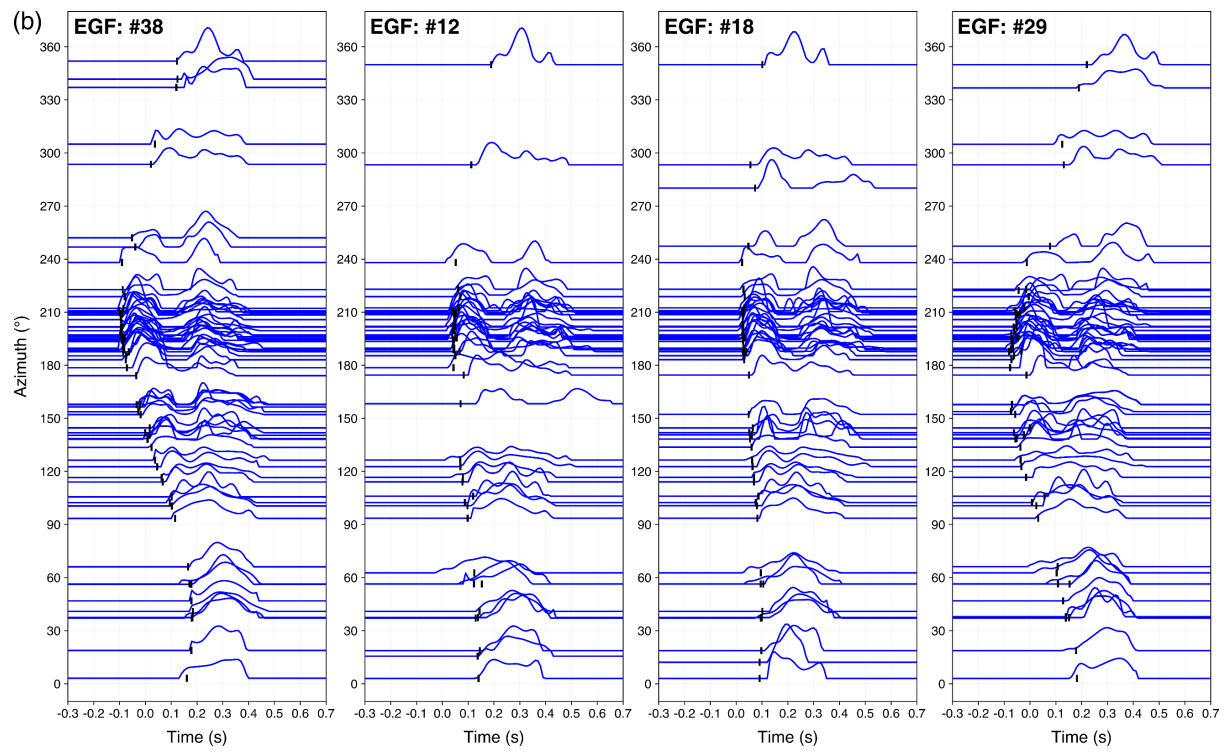


Figure S2b. Direct S-phase mainshock RSTFs obtained using four different EGF candidates (no. 38, 12, 18, and 29). The details are the same as in (a).

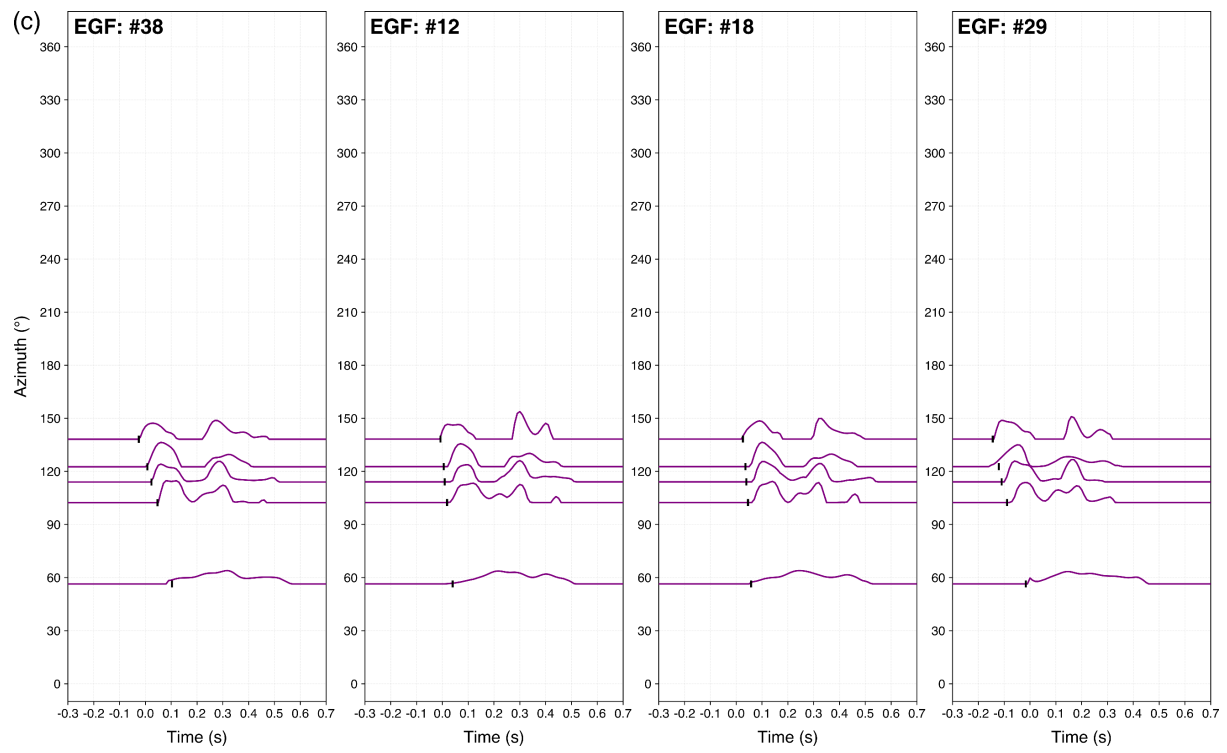


Figure S2c. The SmS -phase mainshock RSTFs obtained using four different EGF candidates (no. 38, 12, 18, and 29). The details are the same as in (a).

(a)



Figure S3a. Comparison of observed mainshock P waveforms (red) and synthetic waveforms (black), reconstructed by convolution of EGFs and RSTFs. Blue labels indicate stations used to construct the slip model.

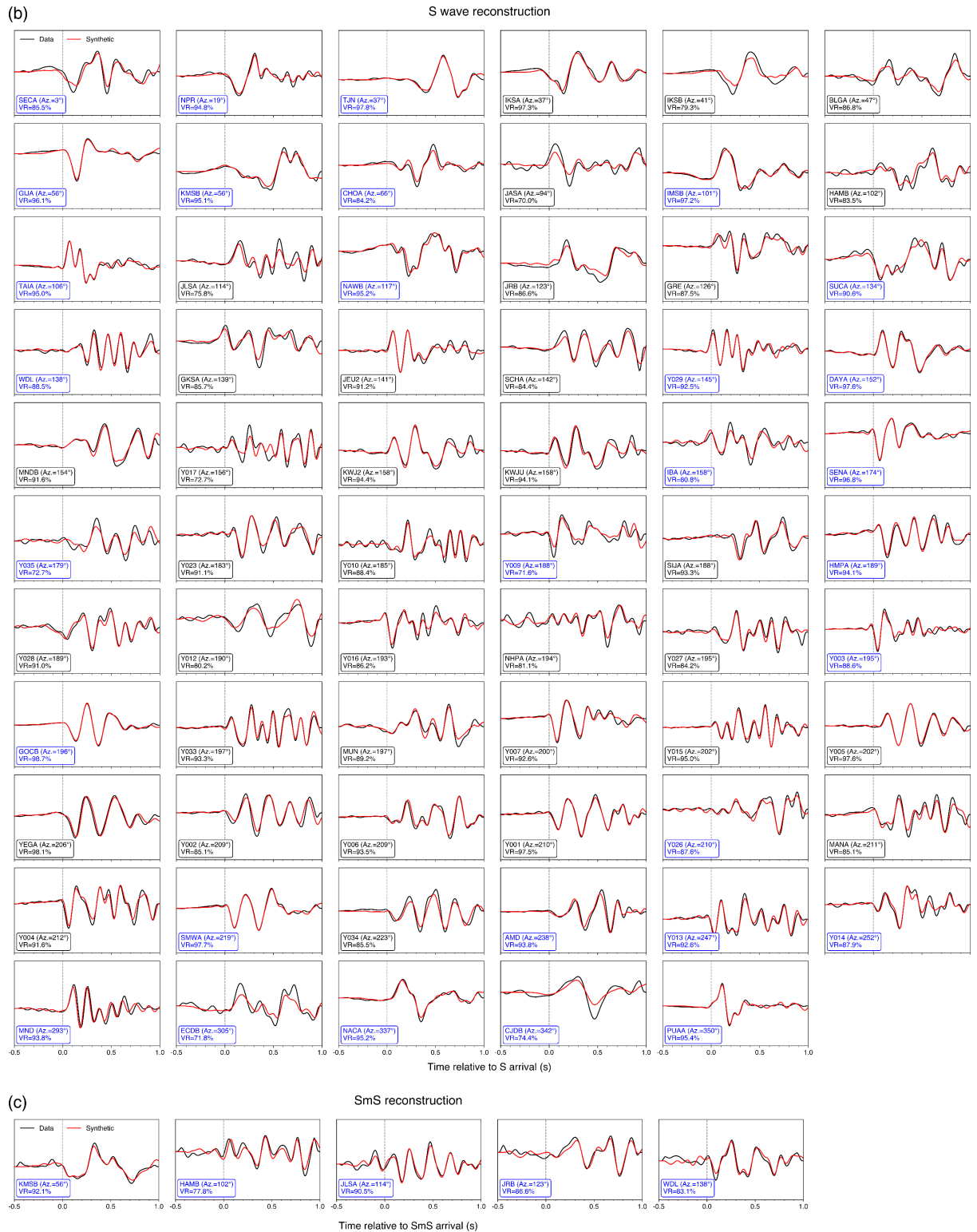


Figure S3b, c. Waveform comparisons for the (b) direct S-phase and (c) SmS-phase. The color coding is identical to that described in (a).

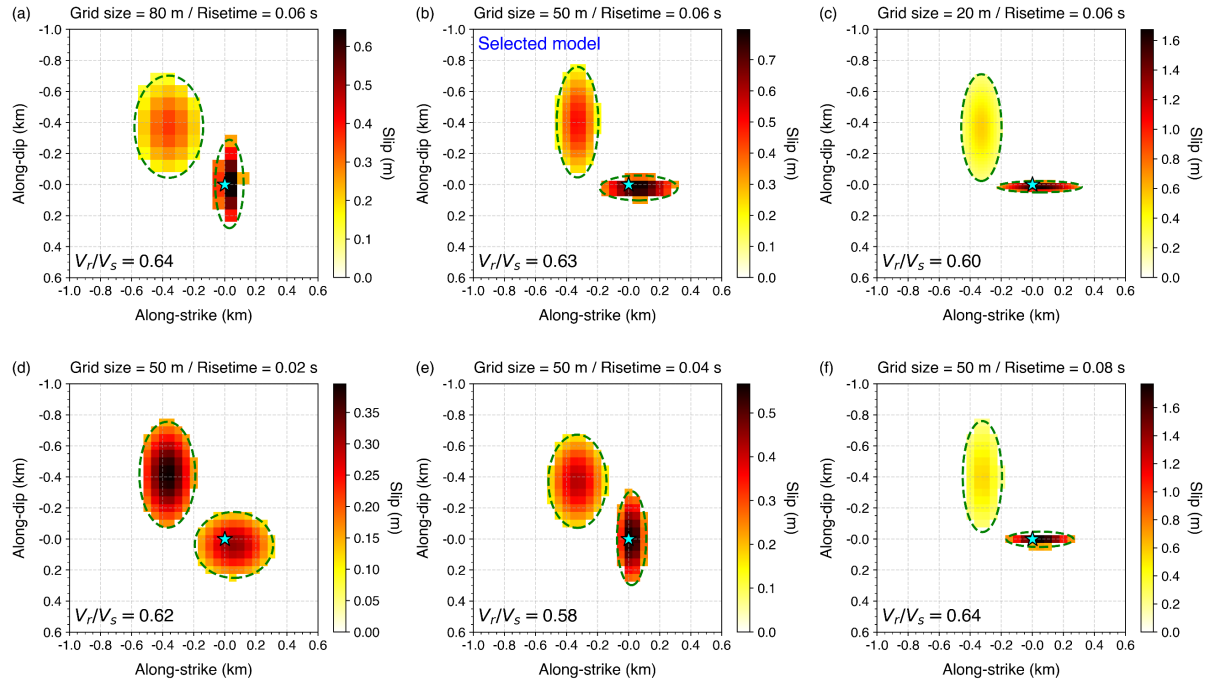


Figure S4. The best-fitting two-patch elliptical models obtained under different assumptions of subfault grid sizes and risetimes. (a)–(c) Results for grid sizes of 80 m, 50 m, and 20 m with a fixed risetime of 0.06 s. (d)–(f) Results for risetimes of 0.02 s, 0.04 s, and 0.08 s with a fixed grid size of 50 m.

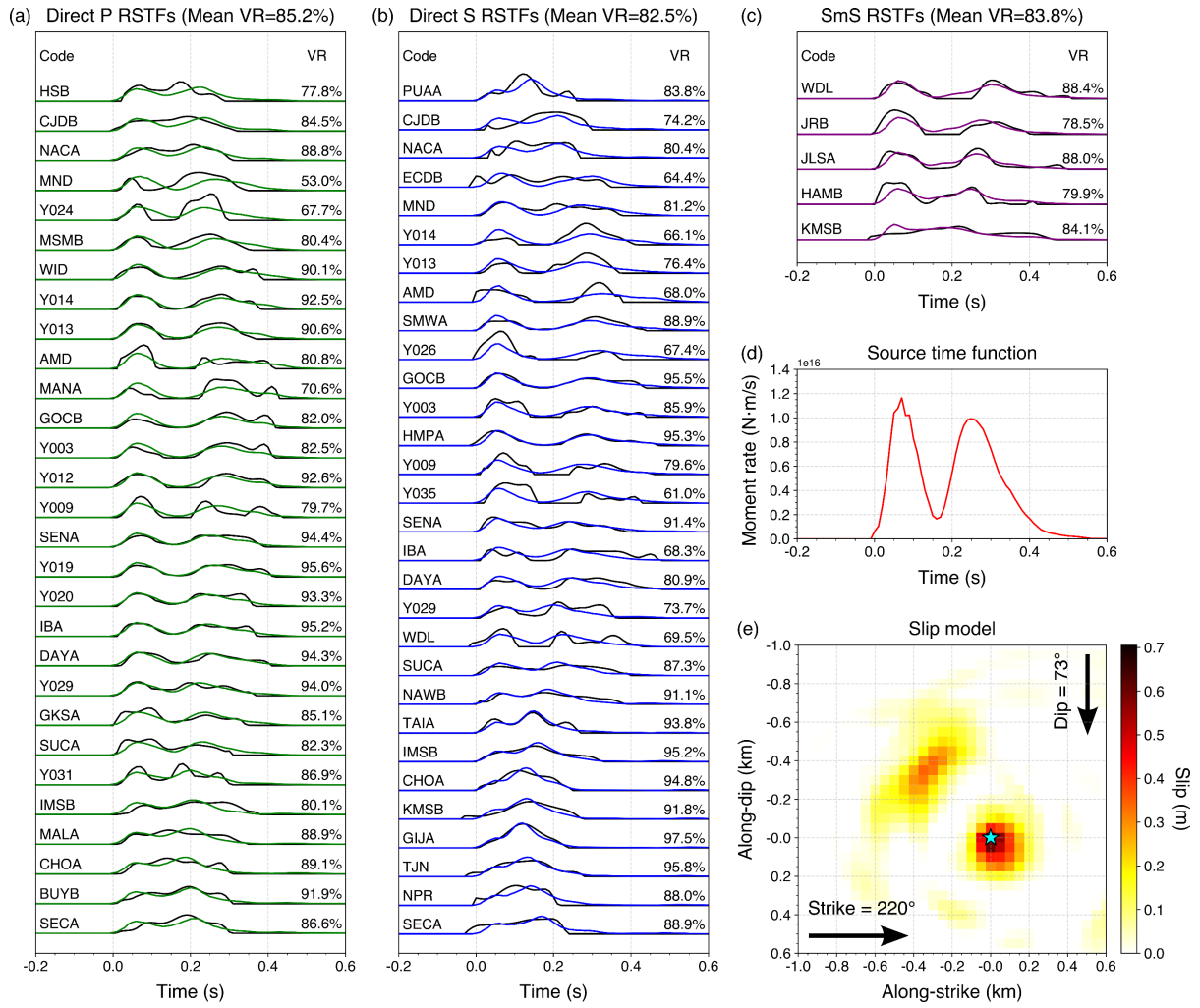


Figure S5. Comparisons between the observed and the synthetic ASTFs forward modeled from the linear inversion slip model are shown for (a) direct P , (b) direct S , and (c) SmS phases. All ASTFs are aligned at their origin times ($t = 0.0$ s) and normalized by the seismic moment. The variance reductions between the observed and the synthetic ASTFs for individual stations are annotated. (d) Source time function representing the overall rupture process. (e) The inverted slip model is plotted on the mainshock fault plane. The cyan star denotes the hypocenter.

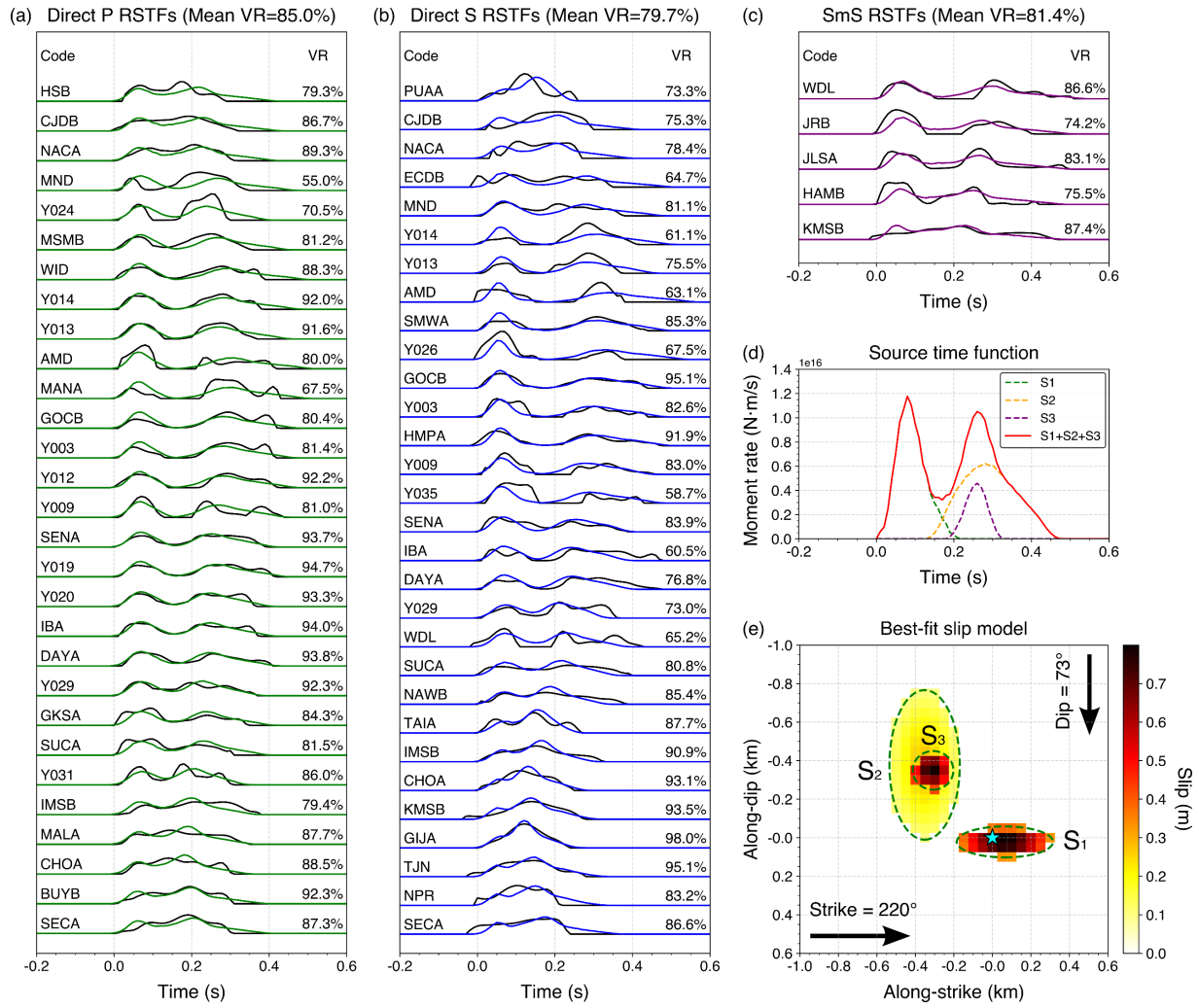


Figure S6. Comparisons between the observed and synthetic ASTFs forward modeled from the best-fit three-patch model, shown for (a) direct P , (b) direct S , and (c) SmS phases. All ASTFs are aligned at their origin times ($t = 0.0$ s) and normalized by the seismic moment. Variance reductions (VRs) between the observed and synthetic ASTFs for individual stations are provided as annotations. (d) The source time function representing the overall rupture process. Contributions from the first (S_1), second (S_2), and third (S_3) patches are plotted as green, yellow, and purple dashed lines, respectively. (e) The best-fit three-patch model is shown on the mainshock fault plane, with the cyan star denoting the hypocenter.

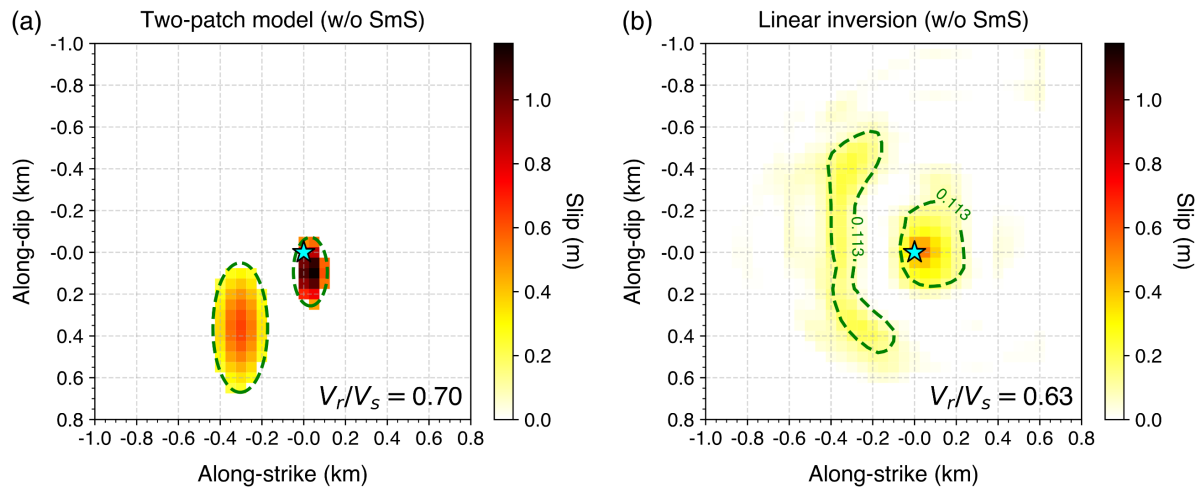


Figure S7. (a) Two-patch elliptical model and (b) linear inversion model obtained without incorporating *SmS* phases. Green dashed contours indicate 20% of the peak slip in the linear inversion.

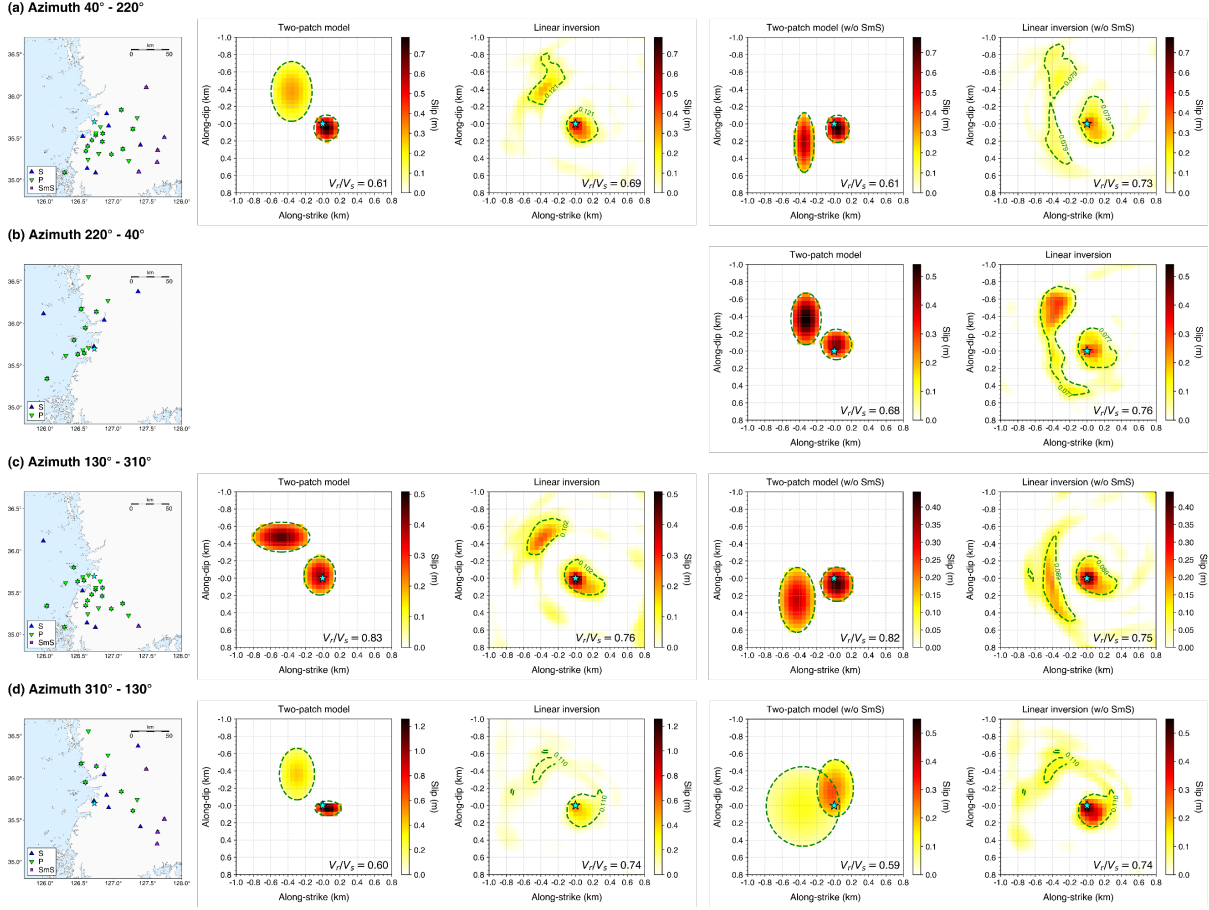


Figure S8. Effect of azimuthal coverage on rupture model resolution. Inversion results for four representative 180° azimuth sectors are shown. For each sector, the station configuration, phase types, and resulting two-patch elliptical and linear inversion models, both with and without *SmS* phases, are shown. The *SmS* phase is absent in $220^\circ - 40^\circ$ azimuth range in panel (b). To suppress unrealistically elongated patches in the elliptical inversion, a penalty term on patch aspect ratio is added to the misfit function: $\alpha[(\log_{10}(a_1/b_1))^2 + (\log_{10}(a_2/b_2))^2]$, with $\alpha = 0.1$. The linear slip inversion was performed by determining the optimal rupture velocity, while the rise time was fixed at 0.05 s, as determined from the analysis applied to the full dataset. Green dashed contours indicate 20% of the peak slip in the linear inversion, which broadly correspond to the elliptical patch boundaries.

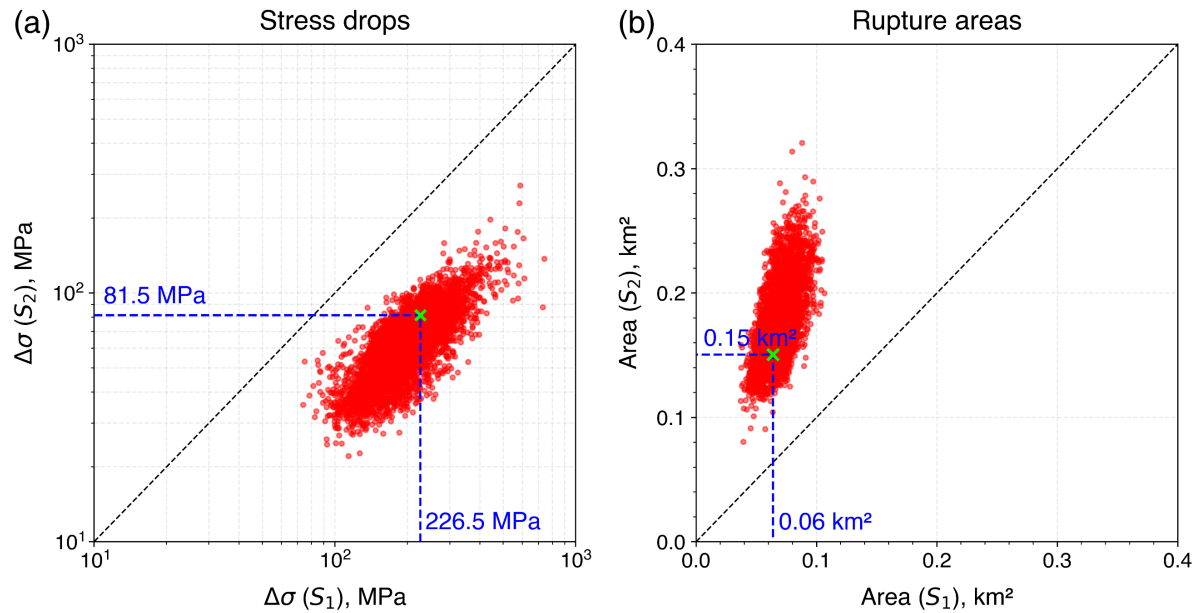


Figure S9. (a) Estimated stress drops of subevents S₁ and S₂ based on the elliptical crack model (Eshelby, 1957; Kaneko and Shearer, 2015). Green crosses indicate the best-fitting inversion result, while red dots represent estimates from the NA solution ensemble. (b) Estimated rupture areas of S₁ and S₂, using the same symbol conventions as in (a). Black dashed diagonal lines in both panels represent the 1:1 reference line.

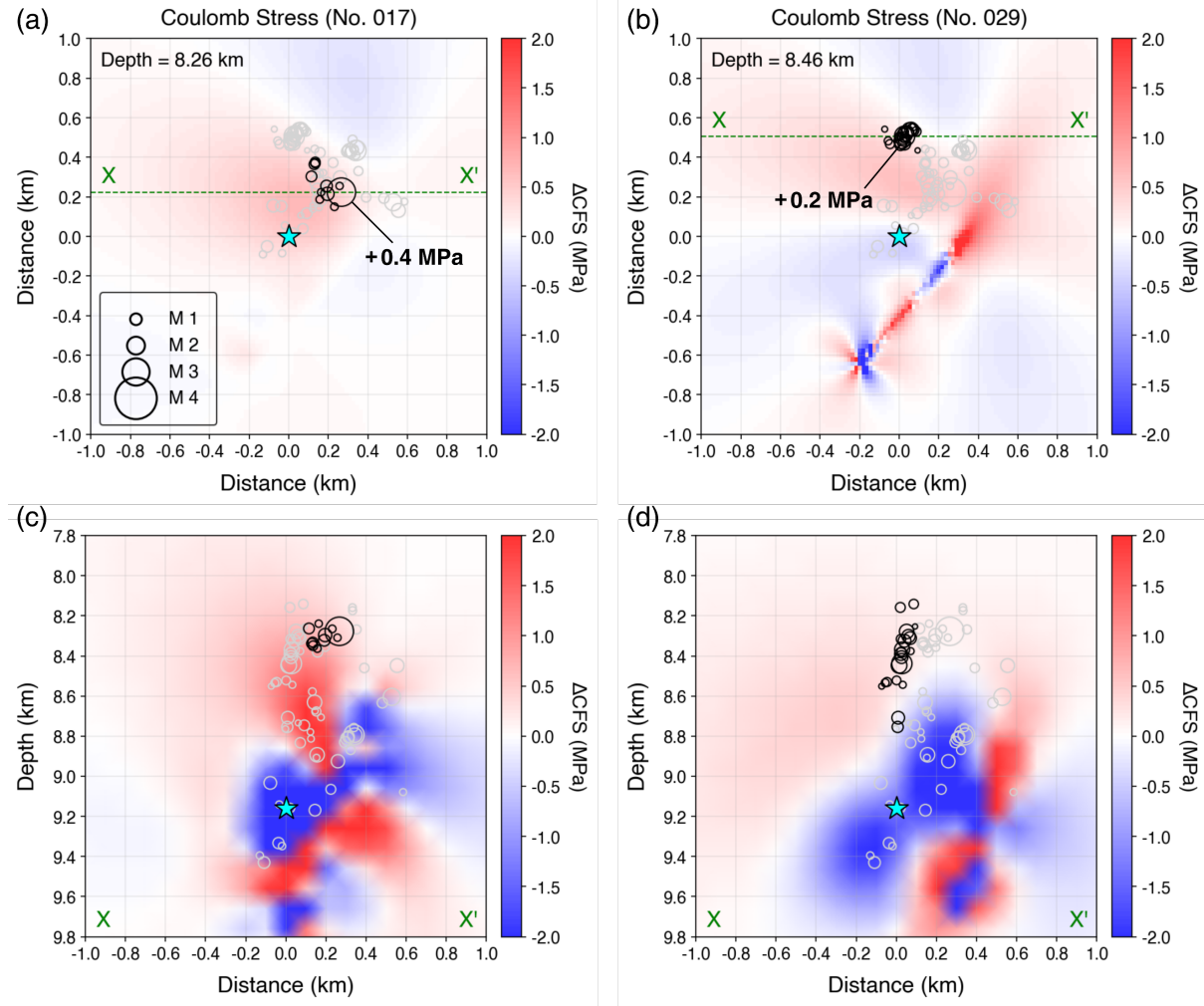


Figure S10. (a) Coulomb failure stress change (ΔCFS) calculated for the receiver fault of event 17, assuming (strike, dip, rake) = $(201^\circ, 32^\circ, 144^\circ)$ at 8.26 km depth. The input mainshock source model is from linear slip inversion, and the mainshock hypocenter is shown as a cyan star. Events associated with the target fault plane are shown as black circles, while other events are shown as gray circles. (b) Same as (a), but for the receiver fault of event 29, assuming (strike, dip, rake) = $(212^\circ, 73^\circ, -166^\circ)$ at 8.46 km depth. (c) Cross-section of ΔCFS along the X – X' line in (a). (d) Cross-section of ΔCFS along the X – X' line in (b).

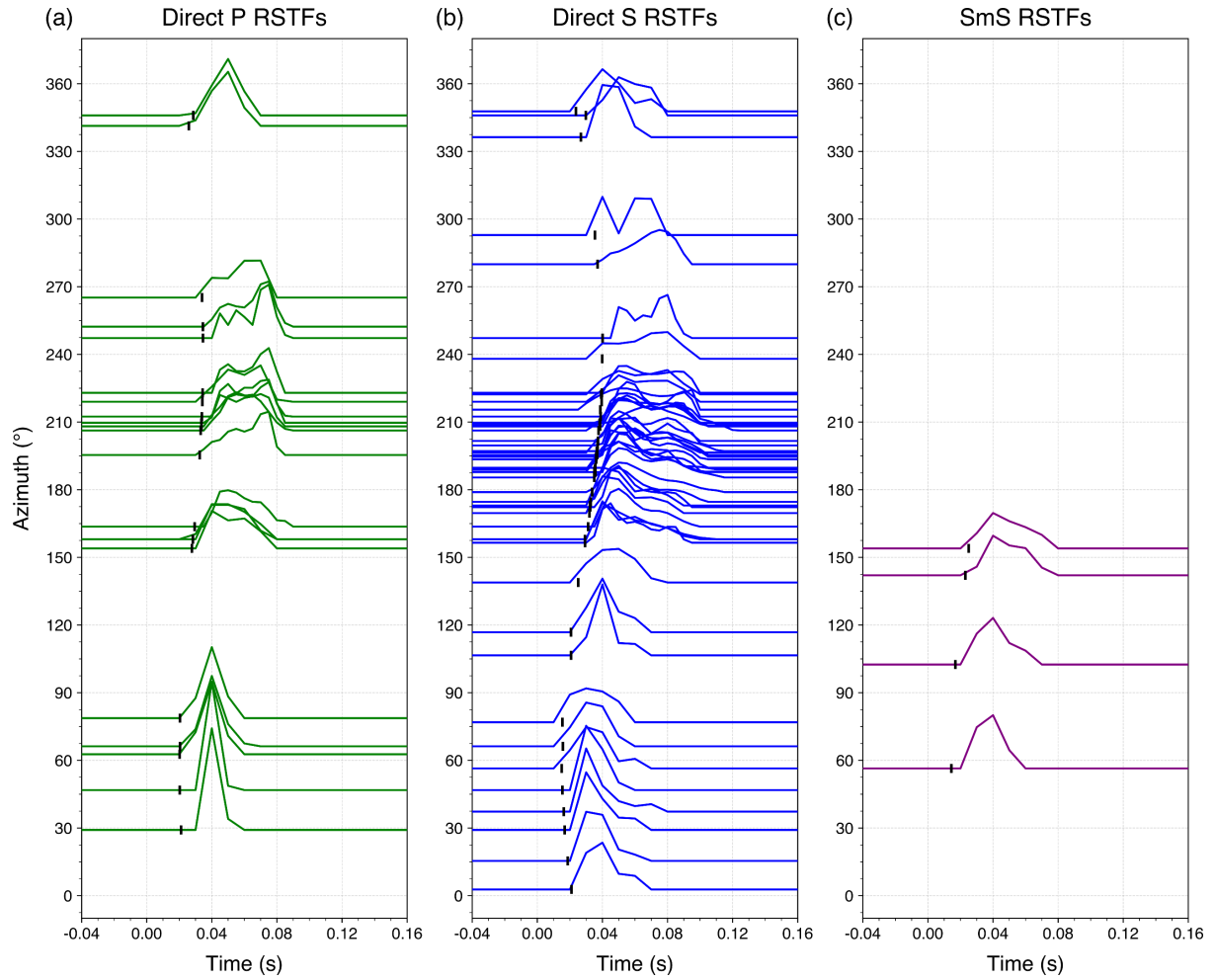


Figure S11. The RSTFs obtained from the target (no. 17) – EGF (no. 11) pair for (a) direct P , (b) direct S , and (c) SmS phases that meet the quality criteria. The RSTFs are aligned by station azimuth and normalized by the seismic moment. Black vertical bars mark the theoretical differential times calculated based on the relative location between the mainshock and the EGF event.

Table S1. Catalog of the 2024 Buan, Korea, earthquake sequence.

ID	Date Time (yyyy/mm/dd hh:mm:ss.ss)	Latitude ($^{\circ}$ N)	Longitude ($^{\circ}$ E)	Depth (km)	M_L^*	H error (km)
1	2024/06/11 22:58:32.38	35.6960	126.7212	8.58	0.5	0.3
2	2024/06/11 23:26:49.96	35.6998	126.7233	9.16	4.8	0.2
3	2024/06/11 23:32:16.52	35.6989	126.7251	8.39	1.3	0.2
4	2024/06/11 23:34:23.86	35.6979	126.7235	7.53	0.8	0.3
5	2024/06/11 23:39:49.89	35.6975	126.7211	8.74	0.9	0.3
6	2024/06/11 23:40:36.29	35.6956	126.7199	8.04	0.6	0.4
7	2024/06/11 23:42:11.24	35.7031	126.7234	7.86	1.5	0.2
8	2024/06/11 23:50:16.37	35.7013	126.7257	8.40	0.9	0.3
9	2024/06/11 23:53:12.75	35.6976	126.7234	7.73	1.0	0.3
10	2024/06/11 23:54:30.96	35.6966	126.7212	8.23	0.7	0.3
11	2024/06/11 23:56:12.19	35.6990	126.7232	7.90	1.3	0.2
12	2024/06/12 00:12:18.22	35.7003	126.7240	8.36	1.5	0.2
13	2024/06/12 00:23:50.72	35.6992	126.7202	8.16	0.9	0.3
14	2024/06/12 01:00:34.12	35.6966	126.7260	7.99	0.7	0.3
15	2024/06/12 04:14:22.22	35.6965	126.7213	8.18	0.8	0.3
16	2024/06/12 04:20:41.92	35.6988	126.7195	7.73	0.7	0.3
17	2024/06/12 04:55:43.25	35.6987	126.7243	7.89	3.1	0.2
18	2024/06/12 05:59:34.75	35.6983	126.7234	8.44	1.5	0.2
19	2024/06/12 08:52:33.27	35.6982	126.7213	8.53	1.2	0.3
20	2024/06/14 13:27:58.36	35.6999	126.7208	7.76	0.6	0.3
21	2024/06/14 20:35:11.71	35.6971	126.7213	7.93	0.4	0.3
22	2024/06/15 04:29:52.17	35.7009	126.7260	8.37	1.0	0.2
23	2024/06/18 05:52:02.94	35.6979	126.7237	8.41	1.3	0.3
24	2024/06/21 20:03:19.40	35.6994	126.7225	7.90	0.6	0.3
25	2024/06/28 22:22:12.17	35.7017	126.7223	7.97	1.2	0.2
26	2024/06/30 18:28:44.64	35.7001	126.7208	8.25	1.2	0.3
27	2024/07/01 14:01:22.64	35.6949	126.7192	8.65	1.3	0.2
28	2024/07/03 05:22:22.49	35.7021	126.7228	8.05	1.7	0.2
29	2024/07/03 05:24:43.59	35.7029	126.7237	8.10	2.3	0.2

30	2024/07/03 05:26:47.75	35.6994	126.7205	8.06	1.2	0.3
31	2024/07/03 09:29:30.60	35.7008	126.7210	8.08	1.6	0.2
32	2024/07/16 16:37:48.56	35.7022	126.7227	7.88	1.3	0.2
33	2024/07/16 23:28:31.60	35.7002	126.7215	7.80	1.2	0.3
34	2024/08/24 05:07:49.19	35.7006	126.7221	7.85	1.2	0.2
35	2024/09/26 02:11:10.86	35.6983	126.7286	7.88	1.0	0.2
36	2025/02/02 08:19:08.96	35.7021	126.7245	8.27	1.5	0.2
37	2025/02/07 07:10:24.95	35.7017	126.7288	8.56	1.9	0.2
38	2025/02/13 03:06:51.89	35.7027	126.7264	9.00	2.3	0.1
101	2024/06/11 23:31:23.79	35.6986	126.7211	7.59	0.73	0.3
102	2024/06/11 23:57:37.46	35.7023	126.7235	8.03	0.50	0.3
103	2024/06/12 01:11:16.05	35.7008	126.7176	7.99	-0.07	0.6
104	2024/06/12 04:39:10.45	35.7012	126.7229	7.86	-0.05	0.4
105	2024/06/12 08:25:10.29	35.6947	126.7182	8.12	-0.39	0.4
106	2024/06/13 00:16:40.70	35.7005	126.7215	8.09	0.41	0.3
107	2024/06/14 11:56:37.37	35.6983	126.7195	7.94	0.39	0.3
108	2024/06/15 17:26:42.10	35.6970	126.7207	8.22	-0.37	0.5
109	2024/06/15 23:59:03.49	35.6985	126.7240	8.04	-0.01	0.4
110	2024/06/16 15:01:16.44	35.7017	126.7274	8.35	0.18	0.2
111	2024/07/26 22:45:34.43	35.6966	126.7205	8.82	0.96	0.3
112	2024/07/29 02:56:52.29	35.7031	126.7232	8.31	0.20	0.5
113	2024/08/01 09:00:04.88	35.6983	126.7198	8.16	0.07	0.4
114	2024/09/21 11:08:18.76	35.6983	126.7197	8.08	-0.20	0.4
115	2024/09/27 08:17:49.45	35.6993	126.7254	7.76	0.40	0.3
116	2024/10/07 10:37:00.85	35.7007	126.7187	7.85	0.08	0.3
117	2024/06/11 23:33:08.80	35.6997	126.7247	8.83	-0.27	0.3
118	2024/06/12 00:55:59.14	35.6986	126.7262	8.07	-0.07	0.6
119	2024/06/12 02:15:45.87	35.6976	126.7194	8.35	0.33	0.6
120	2024/06/12 03:18:31.30	35.7016	126.7228	7.90	0.47	0.4
121	2024/06/12 03:44:45.50	35.6979	126.7221	8.23	-0.33	0.5
122	2024/06/12 07:56:55.10	35.6929	126.7182	8.72	-0.09	0.4
123	2024/06/12 09:40:00.94	35.6915	126.7086	8.83	-0.31	1.4

124	2024/06/12 14:35:15.78	35.6949	126.7207	8.55	-0.34	0.9
125	2024/06/14 19:23:48.96	35.6958	126.7210	8.37	-0.57	0.6
126	2024/06/15 15:22:18.57	35.7024	126.7192	8.20	-0.64	0.5
127	2024/06/16 15:24:19.70	35.7023	126.7270	7.84	-0.85	0.7
128	2024/06/21 22:24:22.88	35.6991	126.7275	8.05	0.48	0.3
129	2024/06/22 11:44:35.03	35.7011	126.7244	8.10	-0.16	0.4
130	2024/06/23 23:30:40.61	35.6950	126.7189	8.69	-0.09	0.5
131	2024/06/29 16:09:34.24	35.7009	126.7264	8.10	0.06	0.5
132	2024/07/02 16:48:48.36	35.6957	126.7192	8.63	-0.87	1
133	2024/07/03 09:33:07.53	35.6984	126.7198	8.25	0.53	0.6
134	2024/07/10 01:14:29.15	35.7005	126.7272	7.94	0.03	0.4
135	2024/07/12 05:16:57.07	35.6995	126.7244	8.64	0.43	0.4
136	2024/07/15 14:08:56.48	35.6973	126.7323	8.06	0.25	0.6
137	2024/07/19 12:45:32.47	35.7000	126.7310	8.68	-0.19	0.3
138	2024/09/11 14:33:01.45	35.7010	126.7257	8.19	-1.03	0.8
139	2024/09/28 15:06:31.70	35.6978	126.7204	8.38	0.02	0.5
140	2024/10/31 16:02:56.89	35.7009	126.7247	7.99	-0.19	0.7
141	2024/11/06 21:03:49.34	35.6914	126.7133	8.73	-0.84	1.2
142	2024/11/29 12:48:30.01	35.6983	126.7235	8.72	0.98	0.3
143	2024/12/07 14:00:40.38	35.6977	126.7249	8.21	-0.76	0.5
144	2024/12/07 23:22:40.33	35.6974	126.7247	7.89	0.03	0.3
145	2025/01/26 19:21:43.59	35.6977	126.7189	8.90	-0.14	0.4
146	2025/02/18 10:52:54.70	35.6966	126.7207	8.20	-0.58	0.5
147	2025/03/20 02:30:52.48	35.6979	126.7236	8.08	0.01	0.4

Date, time, latitude, longitude, depth and H error are from HYPOINVERSE event location.

* Local magnitudes (M_L) are reported by the Korea Meteorological Administration (KMA) for events with IDs 1 – 38, while relative magnitudes based on peak amplitude ratios between detected and template events are used for IDs 101 – 147.

Table S2. The second-degree moment parameters of event 17 obtained from the inversion

ID	L_c (m)	W_c (m)	τ_c (s)	$ \mathbf{v}_0 $ (km/s)	Dir. Ratio	Rake (°)	θ_c (°)	VR (%)
017	74.3 (66.9, 82.1)*	50.1 (22.5, 72.6)	0.0169 (0.0154, 0.0189)	2.09 (1.42, 2.72)	0.477 (0.380, 0.568)	158.5 (142.3, 175.7)	174.4 (153.5, 193.4) †	82.2

* The 95% confidence intervals from the bootstrap analysis.

† The angle measured counter-clockwise from the strike direction.

References

- Kaneko, Y., and P. M. Shearer (2015). Variability of seismic source spectra, estimated stress drop, and radiated energy, derived from cohesive-zone models of symmetrical and asymmetrical circular and elliptical ruptures, *J. Geophys. Res.: Solid Earth* **120**, no. 2, 1053–1079.
- Kim, S. J., and S. G. Kim (1983). A study on the crustal structure of South Korea by using seismic waves, *Econ. Environ. Geol.* **16**, no. 1, 51–61.
- Eshelby, J. D. (1957). The determination of the elastic field of an ellipsoidal inclusion, and related problems, *Proc. R. Soc. London, Ser. A* **241**, no. 1226, 376–396.